The Astrophysical Journal Letters, 982:L32 (11pp), 2025 March 20 https://doi.org/10.3847/2041-8213/adbb63
© 2025. The Author(s). Published by the American Astronomical Society.
OPEN ACCESS

Spectropolarimetry of SN 2023ixf Reveals Both Circumstellar Material and an Aspherical Helium Core

Manisha Shrestha[1], Sabrina DeSoto[2], David J. Sand[1], G. Grant Williams[1,3], Jennifer L. Hoffman[2], Paul S. Smith[1], Callum McCall[4], Justyn R. Maund[5], Iain A. Steele[4], Klaas Wiersema[6], Jennifer E. Andrews[7], Nathan Smith[1], Christopher Bilinski[1], Peter Milne[1], Ramya M. Anche[1], K. Azalee Bostroem[1,19], Griffin Hosseinzadeh[8], Jeniveve Pearson[1], Douglas C. Leonard[9], Brian Hsu[1], Yize Dong (董一泽)[10], Emily Hoang[11], Daryl Janzen[12], Jacob E. Jencson[13], Saurabh W. Jha[14], M. J. Lundquist[15], Darshana Mehta[11], Nicolás Meza Retamal[11], Stefano Valenti[11], Joseph Farah[16,17], D. Andrew Howell[16,17], Curtis McCully[16], Megan Newsome[16,17], Estefania Padilla Gonzalez[16,17], Craig Pellegrino[18], and Giacomo Terreran[16,17]
[1] Steward Observatory, University of Arizona, 933 North Cherry Avenue, Tucson, AZ 85721-0065, USA; mshrestha1@arizona.edu
[2] Department of Physics & Astronomy, University of Denver, 2112 East Wesley Avenue, Denver, CO 80208, USA
[3] MMT Observatory, PO Box 210065, University of Arizona, Tucson, AZ 85721-0065, USA
[4] Astrophysics Research Institute, Liverpool John Moores University, 146 Brownlow Hill, Liverpool L3 5RF, UK
[5] Department of Physics, Royal Holloway, University of London, Egham, TW20 0EX, UK
[6] Centre for Astrophysics Research, University of Hertfordshire, Hatfield, AL10 9AB, UK
[7] Gemini Observatory, 670 North A'ohoku Place, Hilo, HI 96720-2700, USA
[8] Department of Astronomy & Astrophysics, University of California, San Diego, 9500 Gilman Drive, MC 0424, La Jolla, CA 92093-0424, USA
[9] Department of Astronomy, San Diego State University, San Diego, CA 92182-1221, USA
[10] Center for Astrophysics | Harvard & Smithsonian, 60 Garden Street, Cambridge, MA 02138-1516, USA
[11] Department of Physics and Astronomy, University of California, Davis, 1 Shields Avenue, Davis, CA 95616-5270, USA
[12] Department of Physics & Engineering Physics, University of Saskatchewan, 116 Science Place, Saskatoon, SK S7N 5E2, Canada
[13] IPAC, Mail Code 100-22, Caltech, 1200 E. California Blvd., Pasadena, CA 91125, USA
[14] Department of Physics and Astronomy, Rutgers, the State University of New Jersey, 136 Frelinghuysen Road, Piscataway, NJ 08854-8019, USA
[15] W. M. Keck Observatory, 65-1120 Māmalahoa Highway, Kamuela, HI 96743-8431, USA
[16] Las Cumbres Observatory, 6740 Cortona Drive, Suite 102, Goleta, CA 93117-5575, USA
[17] Department of Physics, University of California, Santa Barbara, Broida Hall, Santa Barbara, CA 93106-9530, USA
[18] Department of Astronomy, University of Virginia, Charlottesville, VA 22904, USA
Received 2024 October 9; revised 2025 February 27; accepted 2025 February 27; published 2025 March 20

Abstract

We present multi-epoch optical spectropolarimetric and imaging polarimetric observations of the nearby Type II supernova (SN) 2023ixf discovered in M101 at a distance of 6.85 Mpc. The first imaging polarimetric observations were taken +2.33 days (60085.08 MJD) after the explosion, while the last imaging polarimetric data points (+73.19 and +76.19 days) were acquired after the fall from the light-curve plateau. At +2.33 days there is strong evidence of circumstellar material (CSM) interaction in the spectra and the light curve. A significant level of intrinsic polarization $p_r = 1.02\% \pm 0.07\%$ is seen during this phase, which indicates that this CSM is aspherical. We find that the polarization evolves with time toward the interstellar polarization level during the photospheric phase, which suggests that the recombination photosphere is spherically symmetric. There is a jump in polarization ($p_r = 0.45\% \pm 0.08\%$ and $p_r = 0.62\% \pm 0.08\%$) at +73.19 and +76.19 days when the light curve falls from the plateau. This is a phase where polarimetric data are sensitive to nonspherical inner ejecta or a decrease in optical depth into the single-scattering regime. We also present spectropolarimetric data that reveal line (de)polarization during most of the observed epochs. In addition, at +14.50 days we see an "inverse P Cygni" profile in the H and He line polarization, which clearly indicates the presence of asymmetrically distributed material overlying the photosphere. The overall temporal evolution of the polarization is typical for Type II SNe, but the high level of polarization during the rising phase has only been observed in SN 2023ixf.

Unified Astronomy Thesaurus concepts: Core-collapse supernovae (304); Type II supernovae (1731); Red supergiant stars (1375); Stellar mass loss (1613); Circumstellar matter (241); Spectropolarimetry (1973); Polarimetry (1278)

1. Introduction

Stars with masses greater than 8 $M_\odot$ end their lives as explosive core-collapse supernovae (CCSNe). Hydrogen-rich SNe, also known as Type II SNe,[20] are the most common type of CCSNe (W. Li et al. 2011; N. Smith et al. 2011) and are thought to be explosions of red supergiant (RSG) stars. Direct imaging of SN sites has confirmed the progenitors of Type II SNe to be RSGs (e.g., S. J. Smartt 2015; S. D. Van Dyk 2017).

[19] LSST-DA Catalyst Fellow.

[20] Here we refer only to Types IIP and IIL, not Types IIn, IIb, or other peculiar subtypes.

Original content from this work may be used under the terms of the Creative Commons Attribution 4.0 licence. Any further distribution of this work must maintain attribution to the author(s) and the title of the work, journal citation and DOI.

These transients provide a unique opportunity to probe massive star evolution and its impact on galaxy environments via the formation and distribution of heavy elements. However, there are still critical gaps in our knowledge. Direct observations of mass loss during the final stages, the last months to years before the explosion, are complicated and poorly understood (N. Smith 2014). Increasing evidence from spectroscopy in the form of narrow spectral emission lines from high-ionization states ("flash spectroscopy"; A. Gal-Yam et al. 2014; O. Yaron et al. 2017; R. J. Bruch et al. 2021; K. A. Bostroem et al. 2023; M. Shrestha et al. 2024) and from early light-curve numerical modeling (V. Morozova et al. 2017, 2018) points to brief but extreme precursor mass-loss events producing significant circumstellar material (CSM) in otherwise normal SNe II.

A powerful way to probe both the properties of the CSM and the explosion mechanism is via polarimetric observations during the different phases of the SN evolution. The free electrons in the CSM surrounding the SN scatter the photons from the photosphere, which produces polarization. The polarization of the scattered photons carries the imprint of the scattering medium. In the case of spectropolarimetry, the large-scale asymmetries of the scattering medium create continuum polarization, while line polarization effects are caused by smaller-scale line-specific phenomena such as clumps. Hence, polarimetry is effective in deducing the geometric structure of the SN ejecta as well as its CSM. For a detailed review of SN polarimetry, refer to D. C. Leonard et al. (2006), L. Wang & J. C. Wheeler (2008), R. Chornock et al. (2010), T. Nagao et al. (2019), C. Bilinski et al. (2024), and T. Nagao et al. (2024). Polarimetry of SNe thus provides knowledge complementary to standard photometry and spectroscopy. Furthermore, it can provide information about the geometry of unresolved distant objects that is not obtainable with other astronomical techniques.

Observationally, a few Type II SNe have been observed with significant polarization (D. C. Leonard et al. 2001, 2006; T. Nagao et al. 2019, 2024; S. S. Vasylyev et al. 2023). There is diversity in the observed polarization behavior, with some Type II SNe showing low-level polarization during the plateau, and the polarization tending to peak at the end of the plateau (e.g., D. C. Leonard et al. 2006; T. Nagao et al. 2024). However, in the case of CSM-interacting Type II SNe, early-time polarization observations can help determine the geometry of the CSM, given that significant polarization is expected if the CSM is aspherical, as seen for many Type IIn SNe (e.g., D. C. Leonard et al. 2000; J. L. Hoffman et al. 2008; C. Bilinski et al. 2024). Recently, for the first time, significant polarization during the rising phase has been observed for a nearby Type II SN, SN 2023ixf in M101 (J. R. Maund et al. 2023; S. S. Vasylyev et al. 2023; A. Singh et al. 2024).

SN 2023ixf was discovered on 2023 May 19 at 17:27:15 UTC (MJD 60083.72) in M101 at a distance of 6.85 ± 0.13 Mpc (A. G. Riess et al. 2022) by K. Itagaki (2023). The J2000 coordinates of the SN are R.A. = 14:03:38.562 and decl. = +54:18:41.94 (D. O. Jones et al. 2023) as presented in Table 1. A spectrum taken the same day (MJD 60083.933) classified it as a young Type II SN with flash ionization features (D. A. Perley et al. 2023).[21] The early photometric and spectroscopic evolution of SN 2023ixf has been studied comprehensively (e.g., K. A. Bostroem et al. 2023; D. Hiramatsu et al. 2023; G. Hosseinzadeh et al. 2023; W. V. Jacobson-Galán et al. 2023; N. Smith et al. 2023; J. Zhang et al. 2023; G. Li et al. 2024; A. Singh et al. 2024; E. A. Zimmerman et al. 2024). G. Hosseinzadeh et al. (2023) used early light-curve data to infer an explosion epoch of MJD 60082.75, which we adopt for this Letter.[22] We present the general properties of SN 2023ixf in Table 1.

Table 1
Properties of SN 2023ixf

Parameter	Value
R.A. (J2000)	14:03:38.562
Decl. (J2000)	+54:18:41.94
Explosion epoch (MJD)[a]	60082.75
Distance modulus (μ)[b]	29.178 ± 0.041 mag
Peak magnitude (r_{max})	−18.07 ± 0.04 mag
Time of r_{max} (MJD)	60094.31
T_{pt}[c]	81.50 ± 0.11 days

Notes.
[a] Value from G. Hosseinzadeh et al. (2023).
[b] Value from A. G. Riess et al. (2022).
[c] Estimated value of the time of drop off of the optical light-curve plateau, from B. Hsu et al. (2024).

In addition, early spectropolarimetric observations of SN 2023ixf showed significant polarization ($P_r = 1.02\% \pm 0.08\%$) at the earliest times (+1.4 days, +2.5 days), which began to decline at +3.5 days (S. S. Vasylyev et al. 2023). The flash ionization features along with the behavior of the multi-wavelength early light curves and polarization point to CSM interaction. Here we present optical imaging polarimetry and spectropolarimetry spanning from +2.33 days to +76.19 days after explosion. Note that a subset of the data presented herein was presented by A. Singh et al. (2024). In this Letter, we build on that work by presenting *R*-band imaging polarization values from +2.33 to +76.19 days and spectropolarimetric data with observation dates that span the gap between the results presented in S. S. Vasylyev et al. (2023) and A. Singh et al. (2024). These new data provide us with a complete picture of SN 2023ixf's geometrical evolution.

In this Letter, we present linear spectropolarimetric and imaging polarimetry data for SN 2023ixf, ranging from the brightening phase to the fall from the plateau.[23] The Letter is organized as follows. First, we describe the observations and data reduction in Section 2. This is followed by the calculation of interstellar polarization (ISP) and results from imaging polarimetric and spectropolarimetric observations in Section 3. We compare the results from SN 2023ixf with other SNe in Section 4. Finally, we discuss and conclude in Section 5.

2. Observations and Data Reduction

In this section, we present the data-reduction techniques we followed for the MOPTOP imaging polarimetry and SPOL spectropolarimetry data.

2.1. MOPTOP Data Reduction

We followed up SN 2023ixf using the MOPTOP imaging polarimeter (H. Jermak et al. 2016, 2018; M. Shrestha et al. 2020)

[21] Here we do not differentiate between Types IIP and IIL.

[22] All the phases quoted in this Letter are with respect to this explosion epoch unless otherwise noted.

[23] We only consider linear polarization throughout this work.

Table 2
Log of Polarimetric Observations of SN 2023ixf

Date (UT)	MJD	Phase[a] (days)	Telescope	Instrument	Exposure Time (s)	Airmass	p (R Band) (%)	PA (R Band) (deg)
2023-05-21 01:55:12	60085.08	2.33	LT	MOPTOP	$3 \times 16 \times 0.4$	1.25	1.02 ± 0.07	152 ± 4
2023-05-31 03:36:00	60095.15	12.40	Bok	SPOL	11×960	1.11	0.26 ± 0.07	59 ± 16
2023-06-01 03:36:00	60096.15	13.40	Bok	SPOL	9×720	1.1	0.23 ± 0.07	61 ± 19
2023-06-02 06:00:00	60097.25	14.50	Bok	SPOL	12×720	1.11	0.21 ± 0.07	65 ± 20
2023-06-03 03:36:00	60098.15	15.40	Bok	SPOL	10×720	1.11	0.21 ± 0.07	67 ± 21
2023-06-04 03:36:00	60099.15	16.40	Bok	SPOL	10×720	1.1	0.19 ± 0.07	70 ± 22
2023-06-05 03:50:24	60100.16	17.41	Bok	SPOL	11×720	1.09	0.16 ± 0.07	73 ± 28
2023-06-14[b] 03:50:24	60109.16	26.41	Bok	SPOL	6×720	1.08	0.08 ± 0.07	146 ± 68
2023-06-15[b] 03:36:00	60110.15	27.40	Bok	SPOL	3×720	1.08	0.08 ± 0.07	150 ± 63
2023-06-16[b] 03:36:00	60111.15	28.40	Bok	SPOL	5×720	1.08	0.12 ± 0.07	155 ± 68
2023-06-18[b] 03:36:00	60113.15	30.40	Bok	SPOL	4×720	1.08	0.17 ± 0.07	162 ± 38
2023-06-19[b] 07:40:48	60114.32	31.57	Bok	SPOL	5×720	1.48	0.19 ± 0.07	166 ± 25
2023-07-30 22:33:36	60155.94	73.19	LT	MOPTOP	$5 \times 16 \times 0.4$	1.5	0.45 ± 0.08	22 ± 10
2023-08-02 22:48:00	60158.95	76.19	LT	MOPTOP	$5 \times 16 \times 0.4$	1.7	0.62 ± 0.08	178 ± 7

Notes.
[a] We list phase in days since the explosion epoch of MJD 60082.75.
[b] This data set has been previously published in A. Singh et al. (2024).

mounted on the 2 m Liverpool Telescope (LT; I. A. Steele et al. 2004).[24] MOPTOP is a dual-beam, dual-camera imaging polarimeter with a $7'' \times 7''$ field of view designed for maximum sensitivity for rapidly fading sources such as gamma-ray bursts and SNe. The instrument is equipped with B-, V-, R-, and I-band filters. Imaging polarimetric observations of SN 2023ixf in the B, V, R, and I filters began on 60085.08 MJD (+2.33 days) and ended on 60158.95 MJD (+76.19 days). However, we only present R-band data in this Letter because we have a complete temporal sequence for this filter.

MOPTOP produces 16 different images from each camera, where each frame corresponds to $22.^{\circ}5$ rotation of the wave plate. The data-reduction pipeline running at the telescope performs dark subtraction and flat-fielding. We manually perform aperture photometry to extract background-subtracted counts of the source. These counts are then converted to fractional Stokes parameters $q_{\rm obs}$, $u_{\rm obs}$ and their error via the "two-camera" technique as described in M. Shrestha et al. (2020, their Equations (14) and (17)). We use instrumental Stokes $q_{\rm inst}$ and $u_{\rm inst}$ values from MOPTOP to correct for instrumental effects and obtain the intrinsic values, given by $q_c = q_{\rm obs} - q_{\rm inst}$ and $u_c = u_{\rm obs} - u_{\rm inst}$. These values are used to calculate polarization $p = \sqrt{q_c^2 + u_c^2}$ and position angle $\mathrm{PA} = \frac{1}{2}\arctan\left(\frac{u_c}{q_c}\right)$. There is a polarization bias due to noise in q and u as p is always a positive quantity. We correct for this using the technique presented in S. Plaszczynski et al. (2014). Finally, we subtract the Stokes q and u introduced by ISP. The calculation of the ISP contribution is described in detail in Section 3.1.

2.2. SPOL Data Reduction

We obtained optical (4500–7500 Å) spectropolarimetric data for SN 2023ixf using the CCD Imaging/Spectropolarimeter (SPOL; G. D. Schmidt et al. 1992) mounted on Steward Observatory's 2.3 m Bok telescope (Kitt Peak, AZ) between MJD 60095.15 (+12.40 days) and MJD 60114.32 (+31.57 days; see Table 2). To constrain the instrumental polarization, we observed multiple polarized standards (HD155528, Hiltner 960, and VI Cyg 12) and unpolarized standards (BD+28 4211 and Wolf 1346). We find a low level of instrumental polarization (less than 0.1%) from the observed unpolarized standard stars. Polarized standard star observations were used to calculate the offset in position angle (PA). The data obtained by SPOL were reduced using custom IRAF routines; further details can be found in P. A. Milne et al. (2017) and C. Bilinski et al. (2024). In short, the routine first flat-fields and bias-subtracts each image, which is wavelength calibrated based on He, Ne, and Ar lamp observations taken on the same night. From this, Stokes $q = Q/I$ and $u = U/I$ are extracted. We bin the Stokes parameters to 20 Å (similar to the native resolution of the SPOL setup) to improve the signal-to-noise ratio (S/N). These Stokes parameters are used to calculate the total polarization as $p = \sqrt{q^2 + u^2}$.

As a proxy for R-band imaging data from SPOL observations, we perform an error-weighted average of q and u for all the SPOL data. For consistency with the MOPTOP bias-correction method, we correct for polarization bias introduced by noise in Stokes q and u via the method given by S. Plaszczynski et al. (2014) for the R-band calculations. Observations of a large data set of polarized and unpolarized standard stars, taken for over a decade with SPOL, show a standard deviation of 0.05%. Thus, with these statistics, we adopt a systematic uncertainty of $q = 0.05\%$ and $u = 0.05\%$, as the minimum uncertainty for all the polarization measurements. We subtract ISP contributions as calculated in Section 3.1 from these data. We also calculate the PA following the equation $\mathrm{PA} = \frac{1}{2}\arctan\left(\frac{u}{q}\right)$ and calculate the error in PA by propagating the error.

We note that the SPOL data from 60109.16 to 60114.32 MJD were previously presented by A. Singh et al. (2024). We include them in our analysis, as they have been uniformly reduced with the rest of the SPOL data set presented herein. Due to the relatively low S/N, we only analyze the continuum polarization from these spectra, which we calculate via the error-weighted mean of q and u in the 6000–7000 Å range as a

[24] https://telescope.livjm.ac.uk/TelInst/Inst/MOPTOP/

proxy for the *R*-band data. We use these integrated SPOL data to augment the imaging polarimetry sequence described in Section 2.1. For the presentation of the spectropolarimetric data, we refer the reader to A. Singh et al. (2024).

3. Polarimetry

In this section, we first calculate the polarization contribution from the interstellar medium using two different techniques described in detail in Section 3.1. We then present our results from spectropolarimetric observations and discuss the behavior of the line polarization. Finally, we present the results from imaging polarimetry from MOPTOP and *R*-band continuum polarization estimates from SPOL data.

3.1. Interstellar Polarization

Polarization measurements of a SN are contaminated by ISP due to the intervening dust in the Milky Way and the host galaxy. To extract the intrinsic polarization of SN 2023ixf, we employ two different techniques.

First, we use the dust extinction for the Milky Way and the host galaxy to estimate an upper limit in ISP. For SN 2023ixf, the dust extinction from the Milky Way is $E(B-V)_{\rm MW} = 0.0074$ mag (E. F. Schlafly & D. P. Finkbeiner 2011). To calculate the host-galaxy extinction, N. Smith et al. (2023) used high-resolution spectra to measure the equivalent width of the Na I D absorption lines at the redshift of SN 2023ixf, and found $E(B-V)_{\rm Host} = 0.031$ mag.[25] Thus, the total extinction in the direction of SN 2023ixf is $E(B-V) = 0.0384$ mag. Since the extinction value is greater than 0.01 mag, as noted in R. Skalidis et al. (2018), the upper limit in polarization in the *V* band induced by ISP (corresponding to the case in which the Milky Way and host ISP align in angle) can be calculated using $p^V({\rm ISP}) < 9E(B-V)\%$ (K. Serkowski et al. 1975), assuming the dust in the host galaxy behaves similarly to the dust in the Milky Way. We caution that for low-extinction environments, there are sight lines that show much higher levels of linear polarization than expected from this scaling relation (see R. Skalidis et al. 2018). With $E(B-V) = 0.0384$ mag, we calculate the upper limit of the *V*-band ISP as $p^V({\rm ISP}) < 0.35\%$. This is consistent with the values of 0.35% and 0.37% calculated by S. S. Vasylyev et al. (2023) and A. Singh et al. (2024), respectively.

To calculate the ISP behavior as a function of wavelength, we utilize $p/p_{\rm max} = \exp[-K \ln^2(\lambda_{\rm max}/\lambda)]$, where $p_{\rm max}$ is equivalent to $p^V({\rm ISP})$, the maximum polarization produced at the wavelength $\lambda_{\rm max} = 5300$ Å (an approximation for the *V* band). The value of $\lambda_{\rm max} = 5300$ Å in K. Serkowski et al. (1975) is valid for dust grains similar to Milky Way dust, and we assume an $R_V = 3.1$ extinction law (J. A. Cardelli et al. 1989). In addition, *K* was originally a constant equal to 1.15 (K. Serkowski et al. 1975), but B. A. Wilking et al. (1982) later modified it to be $K = -0.10 + 1.86\lambda_{\rm max}$, which we adopt in this Letter. Here $\lambda_{\rm max}$ is in units of microns, i.e., 0.53 μm.

For the second method, we utilize the polarization associated with the strongest emission line (Hα), as the greater line flux is assumed to dilute and depolarize the continuum (e.g., D. C. Leonard et al. 2000, 2001; T. Nagao et al. 2019; D. C. Leonard et al. 2021; A. Singh et al. 2024). The spectropolarimetry data from SPOL between 2023 June 14 and 2023 June 19 show a prominent Hα feature. We calculated error-weighted averages of the Stokes *q* and *u* values from five different bins ranging from 100 to 200 Å in wavelength centered on the Hα peak. We found similar values (within standard deviations of 0.007 and 0.02 for Stokes *q* and *u*, respectively) as we changed the binning range from 100 to 200 Å. From this method, we calculated $q_{\rm ISP} = -0.08\% \pm 0.05\%$ and $u_{\rm ISP} = 0.10\% \pm 0.05\%$ centered at the Hα peak (an approximation for the *R* band). These values are consistent with the ISP estimate calculated by A. Singh et al. (2024). Our resulting $p_{\rm ISP} = 0.13\%$ value from this method is consistent with the $p^V({\rm ISP}) < 0.35\%$ calculated from the first method. We follow the prescription of K. Serkowski et al. (1975) to calculate the ISP contribution at different wavelengths using $p/p_{\rm max} = \exp[-K \ln^2(\lambda_{\rm max}/\lambda)]$ with $\lambda_{\rm max} = 5300$ Å, $K = -0.10 + 1.86\lambda_{\rm max}$, and $p_{\rm max} = 0.14\%$. We subtract the $q_{\rm ISP}$ and $u_{\rm ISP}$ calculated for each filter from our observed data. We quote and display the ISP-corrected values throughout this work, unless otherwise stated.

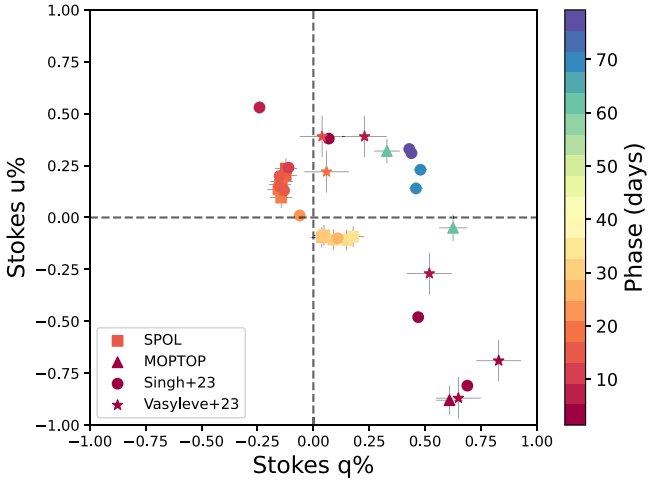

Figure 1. Evolution of *R*-band Stokes *q* and *u* with phase for SN 2023ixf after ISP correction (Section 3.1). The points include data from MOPTOP and SPOL, and data from S. S. Vasylyev et al. (2024) and A. Singh et al. (2024). For the SPOL data we calculated the continuum polarization in the 6000–7000 Å range (Section 2.2).

In Figure 1, we present the ISP-corrected continuum polarization measurements we obtained from the MOPTOP, SPOL, A. Singh et al. (2024), and S. S. Vasylyev et al. (2023) data. While most of these continuum data show intrinsic polarization values, the last few data points during the plateau phase (from +26.41 to 31.57 days) lie very close to the origin of the *q*–*u* plane (∼0.05% for both *q* and *u*), as expected during the photospheric phase.

3.2. Continuum Polarization and Imaging Polarimetry

The calculated continuum polarization and PAs from our observations are presented in Table 2. To see how changes in the polarization correspond to changes in the light curve, we obtained an *r*-band light curve from the Sinistro cameras on Las Cumbres Observatory's robotic 1 m telescopes (T. M. Brown et al. 2013) as part of the Global Supernova Project collaboration (D. A. Howell & Global Supernova Project 2017), which was published in B. Hsu et al. (2024). The *r*-band magnitude peaks at −18.07 mag at 60094.31 MJD. In Figure 2, we present the evolution of the *R*-band polarization with time, along with the *r*-band light curve (top panel). The first and the

[25] There is significant uncertainty in the relation from D. Poznanski et al. (2012).

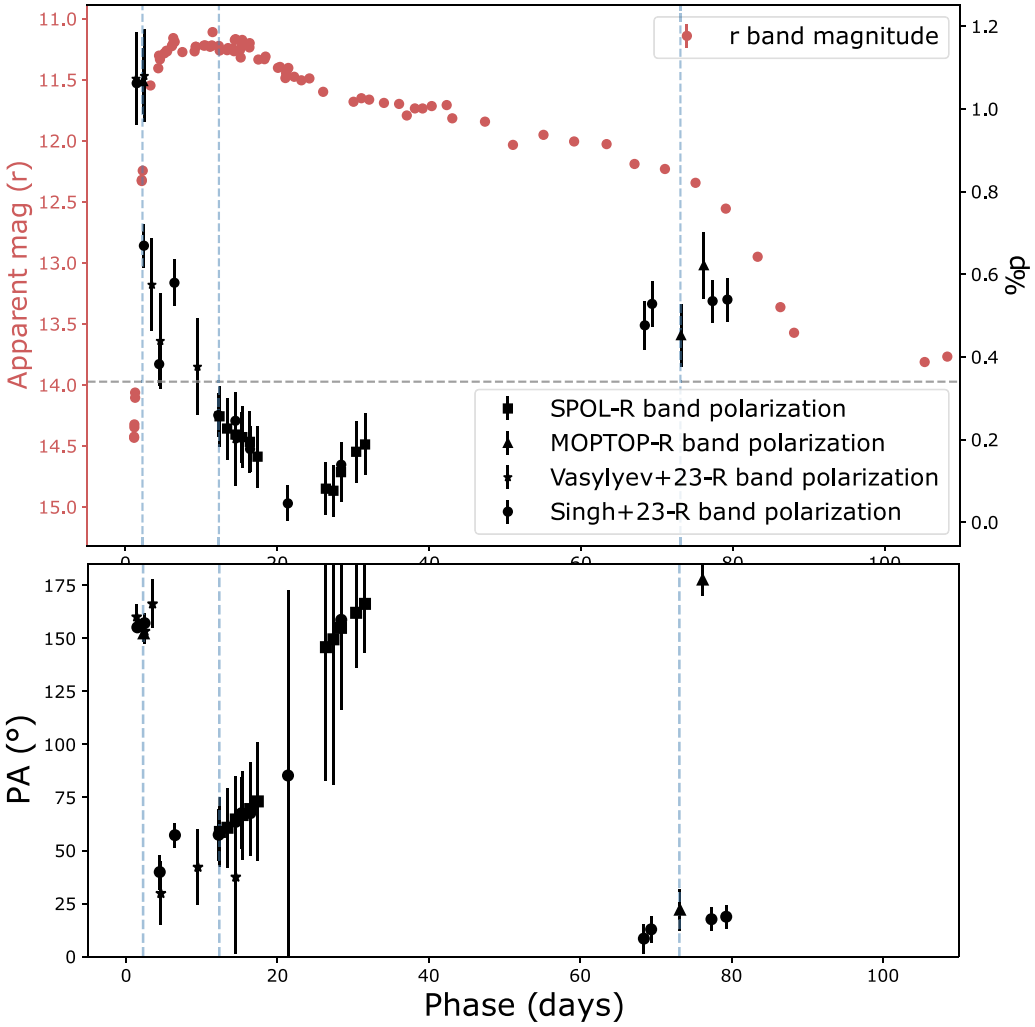

Figure 2. Top: *r*-band apparent magnitude (from Las Cumbres Observatory) and *R*-band polarization with respect to days since the explosion. The light dashed gray line is the maximum ISP in the *R* band as discussed in Section 3. The triangle data points are from MOPTOP observations, and the square symbols are continuum polarization calculated from our SPOL data in the 6000–7000 Å range. Circle and star points represent data from A. Singh et al. (2024) and S. S. Vasylyev et al. (2023), respectively. Polarization detections during the initial rising phase and fall from the plateau suggest asphericity in the CSM and He core, respectively. Bottom: PA with respect to phase for *R*-band data. In both panels, the dashed blue lines represent epochs that are presented in the Figure 3 sketch.

last two polarimetric data points at phases +2.33, +73.19, and +76.19 days are from MOPTOP on the LT, while the data between these points are from SPOL. The bottom panel of the figure shows the corresponding PA values for the polarization measurements above. The dashed gray line represents the ISP upper limit calculated in Section 3.1.

Initially, during the rising phase (+2.33 days), we detect a significant level of continuum polarization from the MOPTOP imaging polarimeter in the *R* band, $p_R = 1.02\% \pm 0.06\%$ and $\mathrm{PA}_R = 152.^{\circ}4 \pm 2.^{\circ}1$. This is consistent with the value of $p_R = 0.82\% \pm 0.07\%$ reported by J. R. Maund et al. (2023) for the same epoch, and other values reported elsewhere during the rising phase (S. S. Vasylyev et al. 2023; A. Singh et al. 2024). In this phase, the SN underwent significant CSM interaction, as seen via the flash features in the early spectra of SN 2023ixf (K. A. Bostroem et al. 2023; W. V. Jacobson-Galán et al. 2023; D. A. Perley et al. 2023; N. Smith et al. 2023; E. A. Zimmerman et al. 2024). Under the assumption of electron scattering, this level of polarization points to a notable break in the spherical symmetry of the CSM, such as an elongated scattering geometry. Thus, we conclude that the CSM close to the progenitor is aspherical, which is also shown by high-resolution spectral data (N. Smith et al. 2023). We also observe a high degree of intrinsic polarization in other filters during this epoch, with $p_B = 0.99\% \pm 0.07\%$, $p_V = 1.21\% \pm 0.08\%$, and $p_I = 0.85\% \pm 0.09\%$ for the *B*, *V*, and *I* filters, respectively. The PA values for these filters are consistent with the *R*-band value, with $\mathrm{PA}_B = 158^{\circ} \pm 4^{\circ}$, $\mathrm{PA}_V = 155^{\circ} \pm 4^{\circ}$, and $\mathrm{PA}_I = 156^{\circ} \pm 6^{\circ}$.

In the first epoch of SPOL data, at the start of the plateau phase (+12.40 days), we see some intrinsic continuum polarization, as also shown in Figures 1 and 2. The PA during this phase is $59^{\circ} \pm 16^{\circ}$, which is close to a 90° rotation compared to our observations during the rise phase (+2.33 days). This 90° PA change was seen by S. S. Vasylyev et al. (2023) for 5–15 days after the explosion, as shown in Figure 2. This continuum polarization decreases over time, and by +17.41 days its value has dropped to $0.16\% \pm 0.07\%$. As we noted in Section 3.1, the continuum polarization reaches even lower levels during days 26–31.

The decline in continuum polarization indicates that the emission is not dominated by the CSM interaction, while the final values near $p = 0.19\%$ suggest that from +17.41 to 31.57 days, when the light curve is well settled in the plateau

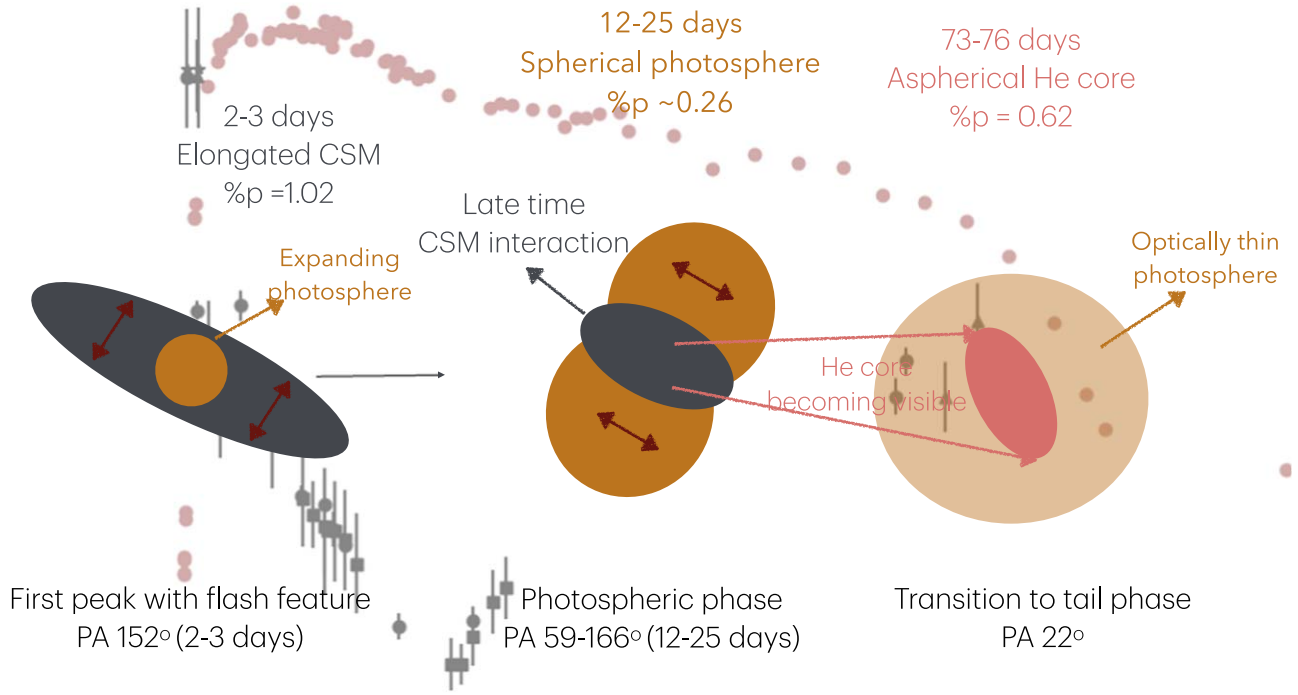

Figure 3. Simplified cross-section sketch, with relative sizes not to scale, of the evolution of the CSM and ejecta geometry of SN 2023ixf based on our imaging and spectropolarimetric data. The background pink data points show the *r*-band apparent magnitude, and the black data points are imaging polarimetric data from Figure 2. The shape of the scattering regions has been exaggerated for better visual representation. Left: elongated CSM (gray region) surrounding the photosphere (orange) with a scattered vector with a (red) PA of 153.°9 for the observation 2–3 days after the explosion. During this phase, there is strong evidence of CSM interaction from the spectra and the light curve. Hence, electron scattering from disk-shaped CSM during this phase produces polarization of 1.02% (Section 3.2). Middle: our first spectropolarimetry data were taken +12.40 days after the explosion, featuring high continuum polarization and inverse P Cygni line features. The continuum polarization is now due to the expanding photosphere (orange), which was constrained by the early CSM but gradually became more spherical during the plateau phase as it swept away the CSM. The inverse P Cygni features are likely due to intervening material from the remnant CSM (gray region) (Section 3.3). Right: during the fall from the plateau, there is another increase in polarization, possibly due to the revealing of an asymmetric He core (red oval) with a different elongation than any earlier structure (Section 3.2).

phase, the intrinsic polarization is very low. These polarization values and their evolution are consistent with those of the imaging polarimetry presented by A. Singh et al. (2024). We note that the PA gradually changes during this phase, as shown in Figure 2 (bottom panel), with a larger error bar in the PA values. We caution that the polarization value during this time range is very low, thus the significance of the change in PA is limited.

By contrast, once the light curve falls from the plateau (+73.19 days; B. Hsu et al. 2024), the continuum polarization increases again to 0.45% ± 0.08% (Figure 2). We observe a similar polarization value for the subsequent epoch at +76.19 days (0.62% ± 0.08%). We note that we also detect significant polarization in other filters at this epoch: $p_B = 1.03 \pm 0.12$, $p_V = 0.98 \pm 0.09$, and $p_I = 0.89 \pm 0.08$ with position angles of $\mathrm{PA}_B = 27° \pm 7°$, $\mathrm{PA}_V = 16° \pm 6°$, and $\mathrm{PA}_I = 16° \pm 5°$ for +73.19 days. For +76.19 days, we find $p_B = 0.86 \pm 0.15$, $p_V = 0.87 \pm 0.11$, $p_I = 0.79 \pm 0.08$, $\mathrm{PA}_B = 172° \pm 10°$, $\mathrm{PA}_V = 177° \pm 8°$, and $\mathrm{PA}_I = 179° \pm 6°$ for the *B*, *V*, and *I* filters, respectively. Additionally, we observe $\mathrm{PA}_R = 22°$, which is a difference of ∼130° from the first epoch of MOPTOP data. This indicates that the mechanism producing polarization during this phase differs from the initial phase. Similar behavior in other Type II SNe has been attributed to an aspherical core being revealed as the outer ejecta become transparent (e.g., D. C. Leonard et al. 2006; T. Nagao et al. 2019, 2021, 2024). However, recent studies (L. Dessart & D. J. Hillier 2011; L. Dessart et al. 2024a) have attributed this solely to a reduction in optical depth. Effectively, it is explained as a purely radiative transfer effect due to a reduction in polarimetric cancellation as the optical depth decreases and single scattering becomes dominant (L. Dessart & D. J. Hillier 2011; L. Dessart et al. 2024a). We also observe some PA rotation as the light curve falls from the plateau, going from 166° ± 25° (+31.57 days) to 22° ± 10° (+73.19 days).

A. Singh et al. (2024) presented time-dependent, ISP-corrected *R*-band polarization of SN 2023ixf, identifying three different peaks at +1.4 days [(1.09% ± 0.05%), (153.4° ± 0.3°)], +6.4 days [(0.54% ± 0.06%), (60.3° ± 1.1°)], and +79.2 days [(0.48% ± 0.05%), (16.9° ± 0.8°)] . We observe the first and last peaks in our data, as well; however, we do not have an observation at +6.4 days. Their observed polarization amplitude and Stokes *q* and *u* evolution are consistent with our data during overlapping epochs.

Figure 4 displays the polarization and PA spectra we observed with SPOL between +12.40 and +17.41 days, with flux spectra and maximum ISP curves overplotted for comparison. At all these epochs, the continuum PA is consistently within a range of 60°–75°, which represents a rotation of almost 90° from our first observation during the rising phase (152°). This behavior is also apparent in Figure 1, where the first and second data points in phase are located in opposite quadrants. This significant rotation could imply that the photosphere has engulfed the CSM region during the peak in the light curve (+12.40 days) and there is a very low level of interaction happening in the CSM region (as suggested by the lack of narrow emission lines in the spectra) as it is swept away. We note that in their simulations, L. Dessart et al. (2024b)

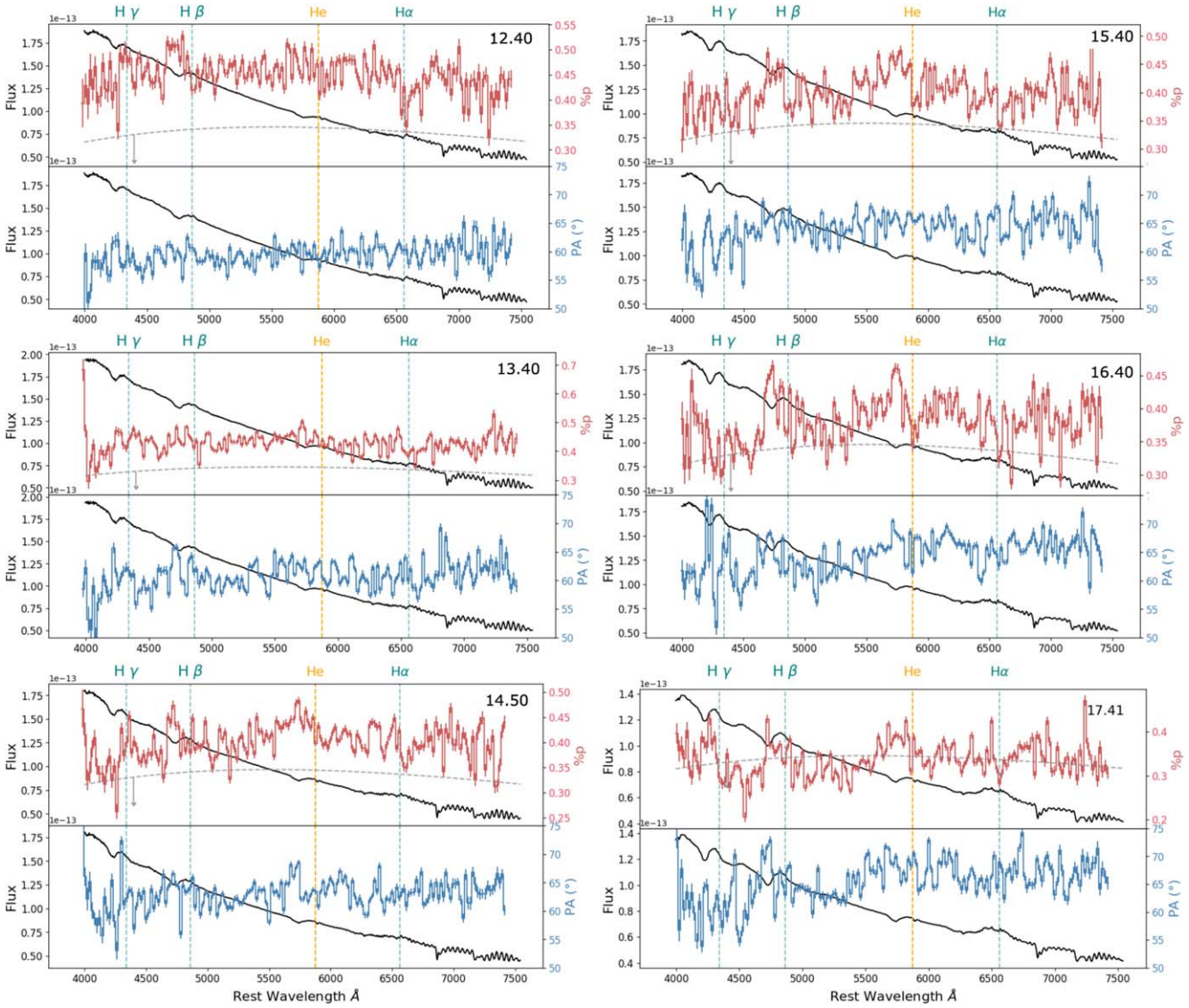

Figure 4. SPOL data from +12.40 days to +17.41 days after the explosion. For each epoch, the top panel contains relative flux (black) and *%p* (red) values and the bottom panel is for the PA (blue), which is binned to 20 Å. Major H and He lines at rest wavelengths are overplotted. The light gray line in the *%p* panel is the maximum ISP estimate as discussed in Section 3. There is a clear continuum polarization in the first two epochs and gradual evolution toward the ISP (<0.35%) with time. The PA is fairly consistent for all the epochs presented here, as shown in Table 2. Finally, clear depolarizations are observed for some lines. The observed continuum polarization above the maximum ISP suggests some level of asphericity in the initial epoch of observation.

also found a drastic change in polarization direction at the conclusion of the strong interaction phase, and similarly attributed it to emission and scattering regions having different spatial distributions.

V. Morozova et al. (2018) studied 20 Type II SNe, and found that a significant fraction in their sample had light-curve peaks that could not be explained by hydrodynamical models using SNEC without CSM interaction; instead, the models with CSM provided a better fit, as shown in Figure 2 of V. Morozova et al. (2018). A similar excess in peak is seen for SN 2023ixf, which indicates that some CSM interaction is present at the time of the light-curve peak and our first SPOL epoch (∼+12 days). The emission is likely not dominated by the CSM interaction as we see during the rise phase, as there are no narrow emission lines during this phase. However, at this epoch, the presence of intrinsic continuum polarization and a flip in PA by 90° from the earlier observation suggests that CSM interaction during the rise produced the "pinched waist" geometry seen in strongly interacting SNe (J. Mauerhan et al. 2014; N. Smith et al. 2015). Scattering by CSM in the pinched waist cancels some Stokes vectors, resulting in a PA rotation of 90°. We note that CSM interaction during this phase has also been invoked for some Type IIn and II SNe (e.g., T. J. Moriya & N. Tominaga 2012; N. Smith et al. 2015). As time passes, the interaction comes to an end and the photosphere is no longer constrained to an elongated shape. The light curve settles to a plateau phase, during which the CSM interaction does not play a major role. Most of the emission is from the photosphere, which retains its earlier preferred angle but approaches a spherical geometry, thus we do not detect significant intrinsic polarization during this phase (see also S. S. Vasylyev et al. 2023).

L. Dessart et al. (2024a) performed 2D polarization radiative transfer calculations to simulate the behavior of the continuum polarization of Type II SNe from 20 to 300 days after the explosion. They used models following the prescription from

their previous work on SN 2012aw (L. Dessart et al. 2021) but with greater kinetic energy and higher ^{56}Ni abundances. In their models, they implemented various bipolar explosions in which the spherical symmetry was broken by adding different materials within ∼30° of the poles. They calculated continuum polarization for the spectral range from 6900 to 7200 Å. They found that the polarization peaks during the fall from the plateau, but the temporal evolution of polarization during the plateau phase is model dependent. Observationally similar diversity in the evolution of polarization during the plateau phase has been seen in Type II SNe (T. Nagao et al. 2024).

Comparing the results from different models in L. Dessart et al. (2024a) with the behavior of our observed polarimetric data for SN 2023ixf, we find that the model e1ni1b1/e1ni1 produces the closest evolution. More information about the different models can be found in Table 1 of L. Dessart et al. (2024a). The bipolar portion of this model, e1ni1b1, has a ^{56}Ni core of 0.009 $M_\odot$ and a ^{56}Ni shell of 0.02 $M_\odot$ that is distributed in the bipolar region within 30° from the pole. This is then paired with e1ni1, which makes up the rest of the scattering region with a ^{56}Ni core of 0.009 $M_\odot$ and no ^{56}Ni shell. We note that the ^{56}Ni mass for SN 2023ixf from observations is higher than the values used in these models (D. Hiramatsu et al. 2023; B. Hsu et al. 2024; T. J. Moriya & A. Singh 2024; A. Singh et al. 2024). From this model (Figure 8, left panel in L. Dessart et al. 2024a), the continuum polarization during the photospheric phase (once the light curve is fully settled to the plateau phase) is close to zero, consistent with SN 2023ixf. Then there is a jump in polarization during the fall from the plateau (Figure 8, left panel in L. Dessart et al. 2024a), similar to the observed data. This behavior was also seen in SN 2004dj (D. C. Leonard et al. 2006). L. Dessart et al. (2024a) attribute the increase in polarization at the end of the plateau phase to the transition from multiple to single scattering, increasing the polarization via reduced cancellation of Stokes parameters. This differs from other interpretations which attribute the change in polarization to an unveiling of the asymmetric inner He ejecta or ^{56}Ni bubbles/plumes during this transition phase (D. C. Leonard & A. V. Filippenko 2001; D. C. Leonard et al. 2006; T. Nagao et al. 2021, 2024). We note that we detect a significant change of ∼20° in PA between +73.19 and +76.19 days, which could indicate there is some inner structure producing this polarization that is not aligned to the scattering region during the plateau phase. We observe this change in PA for all the filters.

3.3. Line Polarization

The polarized spectra displayed in Figure 4 contain various interesting line polarization features. At day +12.40, we observe some depolarization at the Hα (λ6563) and Hγ (λ4341) lines, as shown by the fact that these lines agree in polarization with our ISP upper limit (less polarized than the continuum). We also see clear line polarization in the blueshifted absorption of Hβ (λ4861), as marked in Figure 4. At days +14.50 and +15.40, we see distinct inverse P Cygni profiles in polarization for Hα, Hβ, and He I (λ5876); we present a zoomed-in figure for Hα at this epoch in Figure 5. We observe small PA rotations (<5°) associated with some of the inverse P Cygni profiles in SN 2023ixf, but these are on the same scale as the noise in the PA spectra. We conclude that the PAs associated with these inverse P Cygni profiles during the plateau phase agree well with the overall continuum PA (60°–70°).

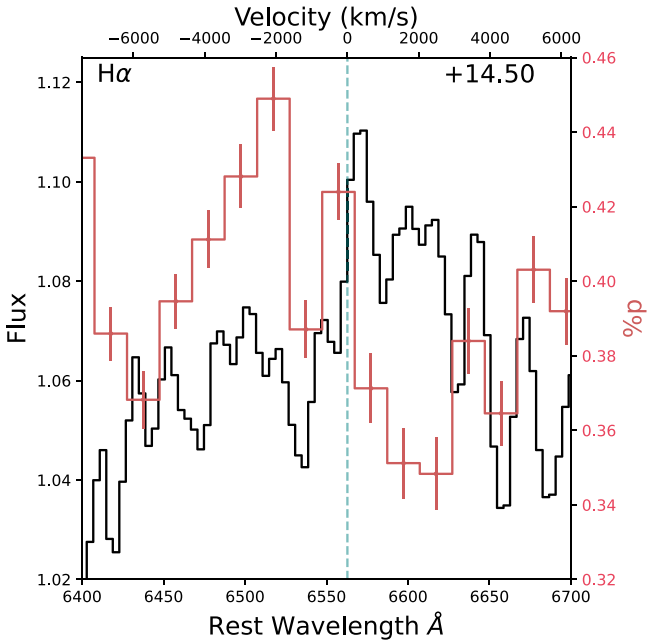

Figure 5. Relative flux (black) and polarization (red, binned to 20 Å) of SN 2023ixf in the region near Hα from our SPOL observation +14.50 days post-explosion. The comparison contrasts the P Cygni profile in the flux spectrum with the inverse P Cygni profile in polarization.

This inverse P Cygni polarization profile is a key indicator of asymmetry in SNe (M. L. McCall 1984; D. J. Jeffery 1991; D. C. Leonard et al. 2001; J. R. Maund 2024). The redshifted emission feature seen in the P Cygni flux profile is produced by resonant scattering of light into our line of sight by ions or atoms in the CSM. Because this resonant scattering polarizes light much less efficiently than electron scattering, it effectively dilutes the continuum polarization. This produces a polarization dip corresponding to the flux increase, as seen in Figure 5. On the other hand, the blueshifted absorption feature seen in the P Cygni flux profile is associated with a peak in polarization, as the region producing this dip in flux blocks or redirects unpolarized light from the central source and thereby increases the fractional polarization. This phenomenon has been seen previously in two Type II SNe, SN 1999em (D. C. Leonard et al. 2001) and SN 2021yja (S. S. Vasylyev et al. 2024). Simply put, these inverse P Cygni profiles are likely due to the intervening material associated with the remaining CSM, which both scatters unpolarized light into our sight line and obscures our view of the emission region. However, the lack of a strong PA rotation across these lines suggests that the remaining CSM during the plateau phase is axisymmetrically distributed with respect to the ejecta (D. J. Jeffery 1991). This is consistent with our picture of the remnant CSM at this stage being aligned with the "waist" of the photosphere.

4. Comparison with Other SNe

We compare the polarization behavior of SN 2023ixf with other Type II SNe in Figures 6 and 7. In Figure 6, we compare the polarization evolution of SN 2023ixf from this work as well as values reported in S. S. Vasylyev et al. (2023) and A. Singh et al. (2024) along with SN 2004dj (D. C. Leonard et al. 2006), SN 2012aw (L. Dessart et al. 2021), and SN 2013ej

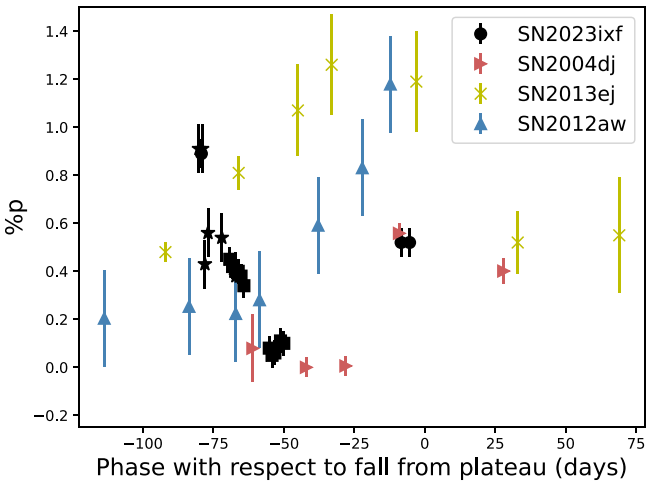

Figure 6. Evolution of the polarization level for various Type II SNe as a function of phase with respect to the fall from plateau (+81.50 days). For SN 2023ixf, different symbols signify data from different instruments: MOPTOP (circle), SPOL (square), and Kast (star; S. S. Vasylyev et al. 2023). Red, blue, and yellow points refer to SN 2004dj, SN 2012aw, and SN 2013ej from D. C. Leonard et al. (2006), L. Dessart et al. (2021), and T. Nagao et al. (2021), respectively.

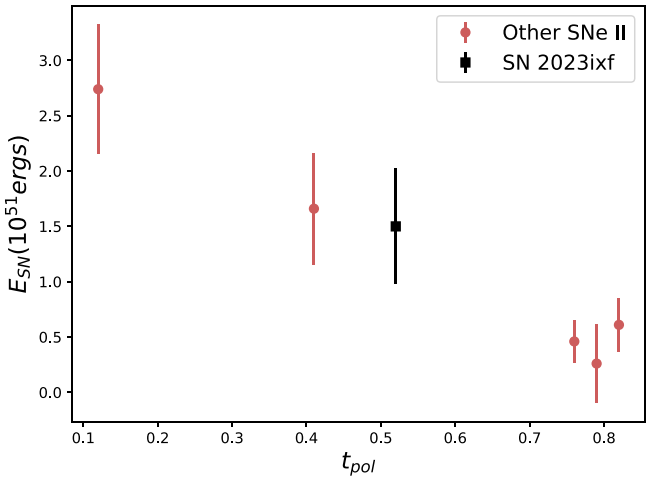

Figure 7. Explosion energy of SNe 2012aw, 2017gmr, 2007aa, 2006ov, and 2004dj from T. Nagao et al. (2024, red) along with SN 2023ixf (black) with respect to t_{pol} (as defined in Section 4). For SN 2023ixf the explosion energy has been estimated to be 1–2 $\times$ 10^{51} erg (D. Hiramatsu et al. 2023; A. Singh et al. 2024), hence we use the center of this range as our explosion energy value and the error bar spans these two values. The calculated value of SN 2023ixf follows the relation seen for other Type II SNe in the literature.

(T. Nagao et al. 2021). In this figure, the phases are days since the fall from the plateau, or T_{pt}, as described in S. Valenti et al. (2016). We chose to present these three because they show a rise in polarization when they fall from the plateau. For both SN 2004dj and SN 2012aw, there are no polarization observations during the very early phase when the brightness is increasing. Thus, we cannot assess whether these SNe showed an initial polarization peak similar to SN 2023ixf. However, for SN 2013ej, T. Nagao et al. (2021) attribute the early polarization detection to CSM interaction.

During the plateau phase, the observed polarization behavior of SN 2023ixf and SN 2004dj is similar and very close to no intrinsic polarization. However, SN 2012aw and SN 2013ej behave differently, with polarization increasing with time and reaching the peak when the light curve falls from the plateau. We note that we do not have data between +31.57 days and +73.19 days, hence the behavior of SN 2023ixf could be similar to SN 2012aw and SN 2013ej.

T. Nagao et al. (2024) examined 15 different Type II SNe and grouped them into three different categories based on polarization values during the photospheric phase. T. Nagao et al. (2024) compares various properties of the SNe in their sample with the characteristic property of the continuum polarization, which is calculated by normalizing the time of the polarization rise to the length of the photospheric phase (t_{pol} = T(polarizationrise)/T(photosphericphase) = 0.52). The authors found a clear correlation between the timing of the polarization rise and the explosion energy, indicating that the explosion asphericity is proportional to the explosion energy. SN 2023ixf falls into the Group 1 category, comprised of SNe which also show a low polarization level at the photospheric phase and an increase in the value during the transitional phase from the photospheric to the tail. According to these criteria, SNe 2008bk, 2007aa, 2006ov, and 2004dj fall in the same category in their sample. However, SN 2012aw falls in Group 2 in T. Nagao et al. (2024), where the polarization increases during the photospheric phase, indicating that the SNe has an aspherical structure in general and not just the He core. We present the relation of the SN explosion energy with respect to t_{pol} in Figure 7, where the red points are from the sample of T. Nagao et al. (2024) and the black point is SN 2023ixf. We use an explosion energy of 1.5 $\times$ 10^{51} erg, the midpoint of the range from A. Singh et al. (2024), for SN 2023ixf, and find behavior consistent with respect to the sample.

Overall, SN 2023ixf behaves similarly to other H-rich SNe, as seen in Figure 7. However, due to its proximity and early follow-up, we detect a high level of polarization in the very early phase where the CSM interaction is dominant; such a signature has not been seen before for other normal Type II SNe. The observed early polarization behavior of SN 2023ixf is reminiscent of Type IIn SNe which have longer-lasting CSM interaction. The polarization of these Type IIn SNe is relatively high and persistent, but eventually drops at later times (e.g., J. L. Hoffman et al. 2008; C. Bilinski et al. 2024).

5. Discussion and Conclusions

In this Letter, we present R-band imaging polarimetry and spectropolarimetry observations (and MOPTOP B, V, and I data in Section 3.2) of the nearby Type II SN 2023ixf. Our first imaging polarimetric data were taken +2.33 days after the explosion when flash features are present in the spectra and the light curve is rising to the peak, and the last data point was taken around the time when the photospheric phase ends and the fall from the plateau phase begins, i.e., +76.19 days. The first spectropolarimetric observation was done on +12.40 days and the last was taken on +31.57 days after the explosion. These data provide us with the following main takeaways:

1. During the initial phase (+2.33 days), we detect an intrinsic polarization value of 1.02% $\pm$ 0.12% and a PA of 152° $\pm$ 14°. At this phase there is also strong evidence of CSM interaction from spectroscopic and photometric data. Our detection of intrinsic polarization at this time confirms that the CSM is aspherical, as suggested earlier by N. Smith et al. (2023), S. S. Vasylyev et al. (2023), A. Singh et al. (2024), L. Ferrari et al. (2024), and Q. Fang et al. (2025).

2. Our next data set starts at +12.40 days, which is close to the maximum in the light curve going to the photospheric phase. The intrinsic continuum polarization is (∼0.26% ± 0.07%) and there is a rotation in PA by 90° compared to the +2.33 phase. This could indicate that as the photosphere expands during the rise phase, it is constrained by the CSM and becomes elongated perpendicular to the initial axis in a "pinched waist" geometry. After the peak at +12.40 days, the photosphere gradually engulfs the CSM and becomes more and more spherical, causing the continuum polarization to decrease toward the ISP value as the CSM is swept away. In addition, during the plateau phase, we see inverse P Cygni behavior in the H and He lines, and the PA around these lines is consistent with the continuum PA. These inverse P Cygni profiles can be attributed to intervening remnant material that is obscuring our view from the emission region.
3. At day +73.19 of our observations, when the light curve falls from the plateau, we measure an increase in polarization to 0.45% ± 0.08% and an increase in PA to 22° ± 10°. A similar jump in polarization during this phase has also been seen for other type II SNe in the literature. This jump can be explained in two different ways. First, the H envelope becomes optically thin and we see an aspherical He core. Alternatively, the optical depth of the scattering medium decreases to the point where single scattering is dominant, which in turn increases the polarization. We have a change in PA during the fall from the plateau, and this could indicate that we are observing a scattering medium (possibly the inner He core) that is not in the same orientation as the scattering medium producing light during the plateau phase.
4. We also compare SN 2023ixf imaging polarimetry behavior in the *R* band with other Type II SNe. We find that from the photospheric phase to the plateau falloff phase, SN 2023ixf behaves similarly to other Type II SNe from the literature. However, the early high level of polarization during the rise phase has not been seen before for Type II SNe that are not Type IIn.

To encapsulate the information gathered from our multi-epoch polarimetry data set, we present a simplified sketch of the temporal evolution of SN 2023ixf in Figure 3. The initial polarization peak can be attributed to an aspherical CSM where electron scattering produces a polarization signal perpendicular to the scattering medium. This marks the first detection of high-level polarization at such an early time for any Type II SNe to date. As the photosphere expands, the PA rotates by 90° between the light-curve rise and the light-curve plateau. Apart from the early high level of polarization, we find the general correlation between explosion energy and $t_{\rm pol}$ seen in other observational studies (e.g., T. Nagao et al. 2024) holds for SN 2023ixf. In particular, the behavior from the plateau phase to the fall from the plateau is similar to that previously seen in SN 2004dj. Our work shows that polarimetric observations can provide complementary information to spectroscopic and photometric observations about the SN, its mass-loss history, and its explosion mechanism. Additionally, we show that early polarimetry observations give additional information about the mass loss from massive stars during their final stages of evolution before the explosion. Together, these findings motivate the need for more rapid polarimetry follow-up observations of Type II SNe.

Acknowledgments

We would like to thank the anonymous referee for constructive comments which have improved the work immensely. Time-domain research by the University of Arizona team, M.S. and D.J.S., is supported by National Science Foundation (NSF) grants 2108032, 2308181, 2407566, and 2432036 and the Heising-Simons Foundation under grant No. 2020-1864. Research by Y.D., S.V., N.M.R, D.M., and E.H. is supported by NSF grant AST-2008108. Operation of the Liverpool Telescope on the island of La Palma by Liverpool John Moores University at the Spanish Observatorio del Roque de los Muchachos of the Instituto de Astrofisica de Canarias is financially supported by the UK Science and Technologies Facilities Council (STFC). K.A.B. is supported by an LSSTC Catalyst Fellowship; this publication was thus made possible through the support of grant 62192 from the John Templeton Foundation to LSSTC. The opinions expressed in this publication are those of the authors and do not necessarily reflect the views of LSSTC or the John Templeton Foundation. J.E.A. is supported by the international Gemini Observatory, a program of NSF's NOIRLab, which is managed by the Association of Universities for Research in Astronomy (AURA) under a cooperative agreement with the National Science Foundation, on behalf of the Gemini partnership of Argentina, Brazil, Canada, Chile, the Republic of Korea, and the United States of America. J.A.C.-B. acknowledges support from FONDECYT Regular No. 1220083. S.D. and J.L.H. acknowledge support from NSF award AST-2009996. They also recognize that the University of Denver resides on the ancestral territories of the Arapaho, Cheyenne, and Ute nations and that its history is inextricably linked with the violent displacement of these indigenous peoples. D.C.L. acknowledges support from NSF grant AST-2010001. This work makes use of data taken with the Las Cumbres Observatory global telescope network. The LCO group is supported by NSF grants 1911225 and 1911151. This research has made use of the NASA Astrophysics Data System (ADS) Bibliographic Services, and the NASA/IPAC Infrared Science Archive (IRSA), which is funded by the National Aeronautics and Space Administration and operated by the California Institute of Technology. This research made use of Photutils, an Astropy package for detection and photometry of astronomical sources (L. Bradley et al. 2019). This work made use of data supplied by the UK Swift Science Data Centre at the University of Leicester. Observations reported here were obtained at the MMT Observatory, a joint facility of the University of Arizona and the Smithsonian Institution. This research has made use of the CfA Supernova Archive, which is funded in part by the National Science Foundation through grant AST 0907903.

Facilities: Bok (SPOL), Liverpool:2m (MOPTOP).

Software: Astropy (Astropy Collaboration et al. 2018, 2013, 2022), Photutils (L. Bradley et al. 2019), Matplotlib (J. D. Hunter 2007), Numpy (C. R. Harris et al. 2020), Scipy (P. Virtanen et al. 2020), IRAF (D. Tody 1986, 1993), `lcogtsnpipe` (S. Valenti et al. 2016).

ORCID iDs

Manisha Shrestha https://orcid.org/0000-0002-4022-1874
Sabrina DeSoto https://orcid.org/0000-0003-4829-6499

David J. Sand https://orcid.org/0000-0003-4102-380X
G. Grant Williams https://orcid.org/0000-0002-3452-0560
Jennifer L. Hoffman https://orcid.org/0000-0003-1495-2275
Paul S. Smith https://orcid.org/0000-0002-5083-3663
Callum McCall https://orcid.org/0000-0002-3375-3397
Justyn R. Maund https://orcid.org/0000-0003-0733-7215
Iain A. Steele https://orcid.org/0000-0001-8397-5759
Klaas Wiersema https://orcid.org/0000-0002-9133-7957
Jennifer E. Andrews https://orcid.org/0000-0003-0123-0062
Nathan Smith https://orcid.org/0000-0001-5510-2424
Christopher Bilinski https://orcid.org/0000-0002-8826-3571
Peter Milne https://orcid.org/0000-0002-0370-157X
Ramya M. Anche https://orcid.org/0000-0002-4989-6253
K. Azalee Bostroem https://orcid.org/0000-0002-4924-444X
Griffin Hosseinzadeh https://orcid.org/0000-0002-0832-2974
Jeniveve Pearson https://orcid.org/0000-0002-0744-0047
Douglas C. Leonard https://orcid.org/0000-0001-7839-1986
Brian Hsu https://orcid.org/0000-0002-9454-1742
Yize Dong (董一泽) https://orcid.org/0000-0002-7937-6371
Emily Hoang https://orcid.org/0000-0003-2744-4755
Daryl Janzen https://orcid.org/0000-0003-0549-3281
Jacob E. Jencson https://orcid.org/0000-0001-5754-4007
Saurabh W. Jha https://orcid.org/0000-0001-8738-6011
M. J. Lundquist https://orcid.org/0000-0001-9589-3793
Nicolás Meza Retamal https://orcid.org/0000-0002-7015-3446
Stefano Valenti https://orcid.org/0000-0001-8818-0795
Joseph Farah https://orcid.org/0000-0003-4914-5625
D. Andrew Howell https://orcid.org/0000-0003-4253-656X
Curtis McCully https://orcid.org/0000-0001-5807-7893
Megan Newsome https://orcid.org/0000-0001-9570-0584
Estefania Padilla Gonzalez https://orcid.org/0000-0003-0209-9246
Craig Pellegrino https://orcid.org/0000-0002-7472-1279
Giacomo Terreran https://orcid.org/0000-0003-0794-5982

References

Astropy Collaboration, Price-Whelan, A. M., Lim, P. L., et al. 2022, ApJ, 935, 167
Astropy Collaboration, Price-Whelan, A. M., Sipőcz, B. M., et al. 2018, AJ, 156, 123
Astropy Collaboration, Robitaille, T. P., Tollerud, E. J., et al. 2013, A&A, 558, A33
Bilinski, C., Smith, N., Williams, G. G., et al. 2024, MNRAS, 529, 1104
Bostroem, K. A., Pearson, J., Shrestha, M., et al. 2023, ApJ, 956, L5
Bradley, L., Sipőcz, B., Robitaille, T., et al. 2019, astropy/photutils: v0.6, Zenodo, doi:10.5281/zenodo.2533376
Brown, T. M., Baliber, N., Bianco, F. B., et al. 2013, PASP, 125, 1031
Bruch, R. J., Gal-Yam, A., Schulze, S., et al. 2021, ApJ, 912, 46
Cardelli, J. A., Clayton, G. C., & Mathis, J. S. 1989, ApJ, 345, 245
Chornock, R., Filippenko, A. V., Li, W., & Silverman, J. M. 2010, ApJ, 713, 1363
Dessart, L., & Hillier, D. J. 2011, MNRAS, 415, 3497
Dessart, L., Hillier, D. J., & Leonard, D. C. 2024a, A&A, 684, A16
Dessart, L., Leonard, D. C., Hillier, D. J., & Pignata, G. 2021, A&A, 651, A19
Dessart, L., Leonard, D. C., Vasylyev, S. S., & Hillier, D. J. 2024b, arXiv:2409.13562
Fang, Q., Moriya, T. J., Ferrari, L., et al. 2025, ApJ, 978, 36
Ferrari, L., Folatelli, G., Ertini, K., Kuncarayakti, H., & Andrews, J. E. 2024, A&A, 687, L20
Gal-Yam, A., Arcavi, I., Ofek, E. O., et al. 2014, Natur, 509, 471
Harris, C. R., Millman, K. J., van der Walt, S. J., et al. 2020, Natur, 585, 357
Hiramatsu, D., Tsuna, D., Berger, E., et al. 2023, ApJL, 955, L8
Hoffman, J. L., Leonard, D. C., Chornock, R., et al. 2008, ApJ, 688, 1186
Hosseinzadeh, G., Farah, J., Shrestha, M., et al. 2023, ApJ, 953, L16
Howell, D. A. & Global Supernova Project 2017, AAS Meeting Abstracts, 230, 318.03
Hsu, B., Smith, N., Goldberg, J. A., et al. 2024, arXiv:2408.07874
Hunter, J. D. 2007, CSE, 9, 90
Itagaki, K. 2023, TNSTR, 1, 2023
Jacobson-Galán, W. V., Dessart, L., Margutti, R., et al. 2023, ApJL, 954, L42
Jeffery, D. J. 1991, ApJ, 375, 264
Jermak, H., Steele, I. A., & Smith, R. J. 2016, Proc. SPIE, 9908, 99084I
Jermak, H., Steele, I. A., & Smith, R. J. 2018, Proc. SPIE, 10702, 107024Q
Jones, D. O., French, K. D., Agnello, A., et al. 2023, TNSTR, 1, 2023
Leonard, D. C., Dessart, L., Hillier, D. J., et al. 2021, ApJL, 921, L35
Leonard, D. C., & Filippenko, A. V. 2001, PASP, 113, 920
Leonard, D. C., Filippenko, A. V., Ardila, D. R., & Brotherton, M. S. 2001, ApJ, 553, 861
Leonard, D. C., Filippenko, A. V., Barth, A. J., & Matheson, T. 2000, ApJ, 536, 239
Leonard, D. C., Filippenko, A. V., Ganeshalingam, M., et al. 2006, Natur, 440, 505
Li, G., Hu, M., Li, W., et al. 2024, Natur, 627, 754
Li, W., Leaman, J., Chornock, R., et al. 2011, MNRAS, 412, 1441
Mauerhan, J., Williams, G. G., Smith, N., et al. 2014, MNRAS, 442, 1166
Maund, J. R. 2024, MNRAS, 528, 3875
Maund, J. R., Wiersema, K., Shrestha, M., Steele, I., & Hume, G. 2023, TNSAN, 135, 1
McCall, M. L. 1984, MNRAS, 210, 829
Milne, P. A., Williams, G. G., Porter, A., et al. 2017, ApJ, 835, 100
Moriya, T. J., & Singh, A. 2024, PASJ, 76, 1050
Moriya, T. J., & Tominaga, N. 2012, ApJ, 747, 118
Morozova, V., Piro, A. L., & Valenti, S. 2017, ApJ, 838, 28
Morozova, V., Piro, A. L., & Valenti, S. 2018, ApJ, 858, 15
Nagao, T., Cikota, A., Patat, F., et al. 2019, MNRAS, 489, L69
Nagao, T., Patat, F., Cikota, A., et al. 2024, A&A, 681, A11
Nagao, T., Patat, F., Taubenberger, S., et al. 2021, MNRAS, 505, 3664
Perley, D. A., Gal-Yam, A., Irani, I., & Zimmerman, E. 2023, TNSAN, 119, 1
Plaszczynski, S., Montier, L., Levrier, F., & Tristram, M. 2014, MNRAS, 439, 4048
Poznanski, D., Prochaska, J. X., & Bloom, J. S. 2012, MNRAS, 426, 1465
Riess, A. G., Yuan, W., Macri, L. M., et al. 2022, ApJL, 934, L7
Schlafly, E. F., & Finkbeiner, D. P. 2011, ApJ, 737, 103
Schmidt, G. D., Stockman, H. S., & Smith, P. S. 1992, ApJL, 398, L57
Serkowski, K., Mathewson, D. S., & Ford, V. L. 1975, ApJ, 196, 261
Shrestha, M., Bostroem, K. A., Sand, D. J., et al. 2024, ApJ, 972, L15
Shrestha, M., Steele, I. A., Piascik, A. S., et al. 2020, MNRAS, 494, 4676
Singh, A., Teja, R. S., Moriya, T. J., et al. 2024, ApJ, 975, 132
Skalidis, R., Panopoulou, G. V., Tassis, K., et al. 2018, A&A, 616, A52
Smartt, S. J. 2015, PASA, 32, e016
Smith, N. 2014, ARA&A, 52, 487
Smith, N., Li, W., Filippenko, A. V., & Chornock, R. 2011, MNRAS, 412, 1522
Smith, N., Mauerhan, J. C., Cenko, S. B., et al. 2015, MNRAS, 449, 1876
Smith, N., Pearson, J., Sand, D. J., et al. 2023, ApJ, 956, 46
Steele, I. A., Smith, R. J., Rees, P. C., et al. 2004, Proc. SPIE, 5489, 679
Tody, D. 1986, Proc. SPIE, 627, 733
Tody, D. 1993, in ASP Conf. Ser. 52, Astronomical Data Analysis Software and Systems II, ed. R. J. Hanisch, R. J. V. Brissenden, & J. Barnes (San Francisco, CA: ASP), 173
Valenti, S., Howell, D. A., Stritzinger, M. D., et al. 2016, MNRAS, 459, 3939
Van Dyk, S. D. 2017, RSPTA, 375, 20160277
Vasylyev, S. S., Yang, Y., Filippenko, A. V., et al. 2023, ApJL, 955, L37
Vasylyev, S. S., Yang, Y., Patra, K. C., et al. MNRAS, 527, 3106
Virtanen, P., Gommers, R., Oliphant, T. E., et al. 2020, NatMe, 17, 261
Wang, L., & Wheeler, J. C. 2008, ARA&A, 46, 433
Wilking, B. A., Lebofsky, M. J., & Rieke, G. H. 1982, AJ, 87, 695
Yaron, O., Perley, D. A., Gal-Yam, A., et al. 2017, NatPh, 13, 510
Zhang, J., Lin, H., Wang, X., et al. 2023, SciBu, 68, 2548
Zimmerman, E. A., Irani, I., Chen, P., et al. 2024, Natur, 627, 759